https://doi.org/10.3311/PPme.20363

Periodica Polytechnica Mechanical Engineering, 66(4), pp. 325–335, 2022

FE Micromodel of a Cord-rubber Composite Test Specimen Subjected to Uniaxial Tension

Gyula Szabó[1*], Károly Váradi[1]

[1] Department of Machine and Product Design, Faculty of Mechanical Engineering, Budapest University of Technology and Economics, 3 Műegyetem rkp., H-1111 Budapest, Hungary
[*] Corresponding author, e-mail: szabo.gyula@gt3.bme.hu

Received: 26 April 2022, Accepted: 14 August 2022, Published online: 06 September 2022

Abstract

The aim of this study is to examine displacements, strains and stresses as well as to predict possible failure mechanisms arising at the yarn-matrix level of a test specimen of a railway composite cord-rubber air brake tube undergoing uniaxial tension by microscale modelling.

Furthermore, this paper also aims to verify the material properties of the micromodel of the test specimen.

The micromodel is based on macromodels (by matching the boundary conditions of the micromodels with displacements of the macromodels) created previously by authors of this article. The reinforcing yarns are described by an orthotropic, elastic material model, whereas the matrix has been described by a 2 parameter Mooney-Rivlin model, which all have been validated before by a uniaxial tensile test and a three-point bending test.

Force-displacement curves of the micromodel and experimental results show a considerably good agreement.

Yarns have a less dominant role in the load transfer mechanism of the reinforcement layers, because of the short-yarn reinforced nature of the specimen. Shear strains are high at free yarn ends marking the possible locations of failure initiation in debonding in the shear mechanism of the reinforcement layers. High shear strain values imply that the dominant mode of load transfer is shear in the matrix in the reinforcement layers.

Keywords

filament-wound composite tube, structural analysis, FE micromodel, uniaxial tension

1 Introduction

Composite tubes are widely used in engineering applications because of their high strength-to-weight and stiffness-to-weight ratios [1]. The most widely used manufacturing process of cord-rubber tubes is filament-winding because of high fiber precision, and being well-suited to automation [2]. During operation, composite tubes are most frequently subjected to biaxial tension (when uniaxial tension is combined with internal pressure) [3], and bending, e.g. during braking [4]. The orientation angle of composite reinforcement layers is ±55° in most cases because it is the most beneficial in case of biaxial tension [5].

In engineering practice, composites are most frequently modelled as orthotropic laminates with so-called 'smeared' (homogenized or averaged) material properties considered at macroscale. These models are useful for the overall mechanical characterization of a composite structure with a significant reduction in computational time and modelling time, however, they approximate internal structural response (e.g. pointwise stress distribution) of composite layers inaccurately [6].

In order to gain more accurate pointwise results, micromodels are most oftenly used, which represent a smaller segment of a composite. Displacement coupling technique (also known as 'submodeling') plays an important role in the definition of the boundary conditions of a micromodel by matching the displacements of the boundaries of the micromodel with the nodal displacements arising on the same surfaces in the macromodel [7].

Several examples of the utilization of micromodels are presented below. Violeau et al. [8] have dealt with damage mechanisms in laminated composites by a hybrid strategy (with predefined cracks) regarding three different load cases: transverse loading and shear loading on cross-ply laminates, and a dual notch sample subjected to

Cite this article as: Szabó, G., Váradi, K. "FE Micromodel of a Cord-rubber Composite Test Specimen Subjected to Uniaxial Tension", Periodica Polytechnica Mechanical Engineering, 66(4), pp. 325–335, 2022. https://doi.org/10.3311/PPme.20363

longitudinal strain. They examined the degradation patterns and crack propagation mechanisms in each case.

Llorca et al. [9] have performed multiscale virtual tests on various composite structures. They firstly determined matrix and interface mechanical properties in situ at the micrometer range, then created a structure of simulations taking into account deformation and failure mechanisms at different length scales. They proposed the extension of their strategy by also including functional properties computed by means of molecular dynamics.

Arteiro et al. [10] have predicted failure of composite laminates at micro-, meso- and macrolevels. They analysed ply thickness effects and predicted in-situ strengths at microscale level. At structural level, strength has been determined by the use of analytical and computational fracture approaches. They found that computational mechanics models are appropriate for the prediction of failure and strength, while at structural level, analytical Finite Fracture Mechanics models yield better results in the assessment of brittle fracture.

A special case of micromodels is the 'unit cell' type, which is a square or hexagonal periodical representative volume element, the smallest segment over which a measurement can be made that will yield a value representative of the structure. Xu et al. [11] have developed a macro-meso unit cell model combined with the shell-core structural feature of 3D braided composites. They predicted the elastic constants and micromechanical response. The effects of the braiding angle and the fiber volume fraction of specimens on the elastic properties have been discussed extensively.

Zhang et al. [12] have established a 3D FE mesoscale progressive damage model of a single-layer triaxially braided composite based on the Murakami-Ohno damage theory to analyse damage initiation and progression in fiber tows. Damage development of fiber tows and interlaminar delamination damage of interface have been analysed.

Li et al. [13] have created a a dense but non-intersecting geometry internal unit cell model of 3D five-directional braided composites based on microscopic observations and predicted the effective elastic constants of 3D five-directional braided composites. Their model was proven to be more effective to calculate the mechanical properties of 3D five-directional braided composites with more than 50% fiber volume fraction compared to existing FE models.

Present authors developed a numerical technique previously for macromechanical analysis of a filament-wound cord-rubber composite test specimen subjected to uniaxial tension [14].

In this study, the uniaxial tension process of the test specimen is further investigated by a micromechanical approach in order to examine the mechanical behaviour of composite layers.

2 Materials and methods

2.1 Uniaxial tensile test

The standard test specimen has been subjected to uniaxial tension in a previous study [14].

An illustration of the tensile test of the standard test specimen can be seen in Fig. 1 at the moment when the upper tensile jaws have travelled 19 mm. Uniaxial tension has been carried out in accordance with standard ASTM D638 with a prescribed displacement of 25 mm at a tensile speed of 2 mm/min on a Zwick Z250 tensile test machine. This tensile speed ensures that time-dependent behavior is avoided during the test. Fig. 1 shows signs of yarn-matrix debonding within layers (seen as gaps across the reinforcement layers) at a displacement of 19 mm.

2.2 FE macromodel

In Section 2.2, the FE macromodel of the standard test specimen is reviewed [14], on which the current micromodel is based on.

Cross-section of the composite tube can be viewed in Fig. 2. The inner diameter of the tube is 28 mm, its outer diameter is 44 mm, the thickness of the rubber liners is 2.4 mm. The material coordinate system of the reinforcement layers is cylindrical, the layup is balanced, [+55°/−55°/+55°/−55].

The test specimen has been cut from the tube through its whole thickness, so thickness of the test specimen is 8 mm.

Fig. 1 Uniaxial tensile test of standard test specimen with clearances illustrating debonding at a displacement of 19 mm [14] © 2017 by authors and Scientific Research Publishing Inc.

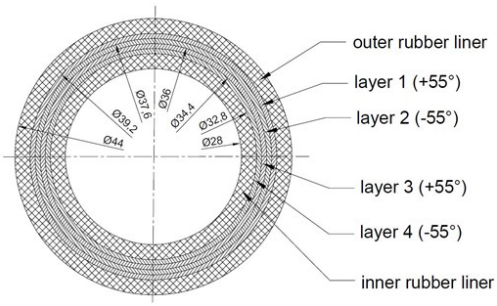

Fig. 2 Cross-section of the composite tube [14] © 2017 by authors and Scientific Research Publishing Inc.

In the FE macromodel, material model of reinforcement layers is transversely isotropic, material properties of the composite layers have been calculated based on rules of mixture [10] and material properties of the components (from material data sheets). Material properties of reinforcement layers are as follows: modulus of elasticity of fibre is $E_f = 2961$ MPa, Poisson's ratio of fibre is supposed to be $\upsilon_f = 0.2$, modulus of elasticity of rubber matrix is $E_m = E_r = 6$ MPa. For the composite layers: $E_1 = 1338$ MPa, $E_2 = E_3 = 19$ MPa, $\upsilon_{12} = \upsilon_{13} = 0.3637$, $\upsilon_{23} = 0.496$, $G_{12} = G_{23} = G_{13} = 6$ MPa [14, 15]. The aforementioned material properties are defined in the material coordinate system, in which:

1. designates yarn direction,
2. designates transverse direction inside the layer,
3. stands for the direction normal to the layer.

Rubber liners, made of EPDM-EVA compound, regarded as incompressible, have been described by a 2 parameter Mooney-Rivlin model with the following parameters: $C_{10} = -0.4982$ MPa, $C_{01} = 1.523$ MPa, $D = 0$ [14].

For the rubber material, the strain energy density function can be written as:

$$W = C_{10} \cdot \left(\overline{I}_1 - 3\right) + C_{01} \cdot \left(\overline{I}_2 - 3\right), \tag{1}$$

where W is the strain energy density function, $\overline{I}_1$ and $\overline{I}_2$ are the first and second invariant of $\overline{B}$, the deviatoric component of the left Cauchy-Green tensor B [16].

By substituting the aforementioned constants to Eq. 1, the parametrized Mooney-Rivlin law for the rubber material is:

$$W = -0.4982\,(\text{MPa}) \cdot \left(\overline{I}_1 - 3\right) + 1.523\ \text{MPa} \cdot \left(\overline{I}_2 - 3\right).$$

These material properties have been validated by the uniaxial tensile tests performed on test specimens and tube samples, the experimental forces showed good agreement with those of the macromodels [14].

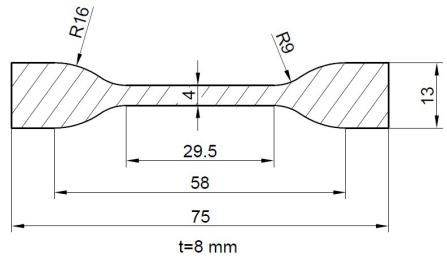

Fig. 3 Dimensions of the test specimen, along with the yarn orientation of *layer 1* (+55°) and thickness of the test specimen *t* [14] © 2017 by authors and Scientific Research Publishing Inc.

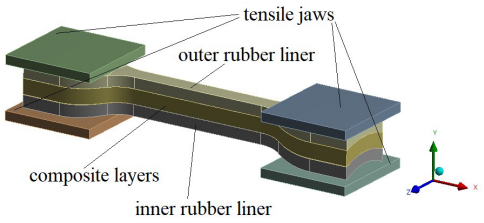

Fig. 4 FE model arrangement of standard test specimen [14] © 2017 by authors and Scientific Research Publishing Inc.

Dimensions and yarn orientation of *layer 1* can be seen in Fig. 3, while FE model arrangement can be viewed in Fig. 4.

Rubber is vulcanized around yarns, so connection of inner and outer rubber liners to reinforcement layers is bonded.

The macromechanical FE simulation consists of 3 time steps. The standard test specimen has been fixed into the left and right tensile jaws in the first and the second timesteps respectively. The tensile jaws are modelled as steel with a modulus of elasticity of $E = 200{,}000$ MPa and a Poisson's ratio of $v = 0.3$. Contacts of the tensile jaws and the test specimen are frictional with a coefficient of friction of 0.8 in order to avoid any slipping [17]. In the third timestep, a prescribed displacement of 25 mm has been applied on the tensile jaws of the right end, while the tensile jaws on the left end hold their position.

2.3 FE micromodel

FE micromodel of the standard test specimen consists of a micromodel cut from the cross-section, in the vicinity of midplane YZ; $-5 < x < 5$ (mm) (Fig. 5) having a length of 10 mm and a width of 4 mm, measured at the middle of the composite layup, containing both the reinforcement layers and the rubber liners (Fig. 6). In the micromodel, yarns and matrix are modeled as solid bodies cut from a geometric model of filament-wound yarn bundle having a winding angle (orientation angle) of 55°. Diameter of the yarns is 0.7 mm

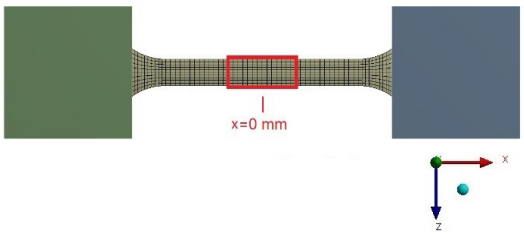

Fig. 5 Position of the micromodel cut from the macromodel-test specimen

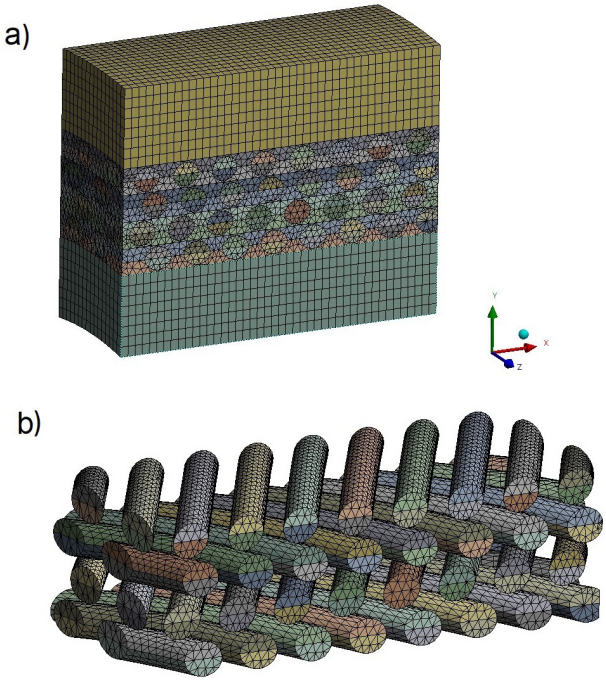

Fig. 6 Meshed geometry of the micromodel of the composite tube test specimen; a) complete model; b) yarn orientation (matrix hidden)

measured on yarns extracted from the tube (Fig. 7(b)). The reinforcement layers have a fiber volume fraction of 45% as in the case of the macromodel [14]. All the yarns and the matrix in the reinforcement layers are split into two segments (Fig. 6(a) and (b)) for better visualization (some results are taken from the boundary of these two half layers).

Yarns are modeled as linear orthotropic (transversely isotropic), with the following material properties: E_1= 2961 MPa, $E_2 = E_3$=20 MPa, $v_{12} = v_{13}$= 0.2, v_{23} = 0.4, $G_{12} = G_{13}$ = 5 MPa, G_{23} = 5 MPa. Modulus of elasticity in material direction 1 E_1 is 2961 MPa (see Section 2.2; for the detailed deduction of E_1, see [14]). Moduli of elasticity E_2 and E_3 are estimated to be 20 MPa, much lower than E_1 as the yarn has little stiffness in direction 2 and 3 due to having a long pitch of twist relative to the thickness of a single fiber (Fig. 7). Shear moduli G_{12}, G_{13} and G_{23} are estimated as the shear moduli of the rubber matrix because interaction of single fibers is slight in the shear mechanism

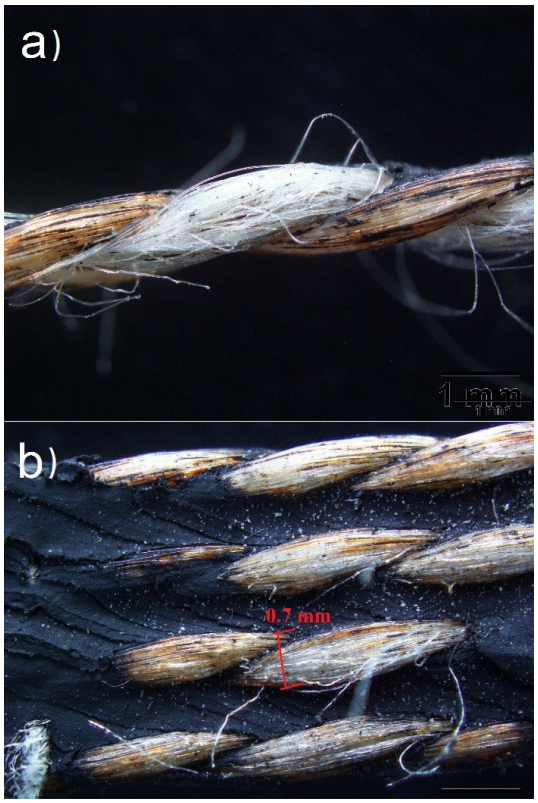

Fig. 7 Microscopic images of reinforcement yarns; a) microscopic image of one yarn; b) microscopic image of yarns embedded in the rubber matrix with the diameter of one yarn indicated in red

of the yarn due to the low thickness of a single fibre and in-plane shear mechanism is affected mostly by matrix properties (Fig. 7(a) and (b)) [18].

Moreover, due to possible inaccuracies regarding the estimation of moduli E_2 and E_3, the case of E_2=E_3=200 MPa has also been investigated.

In these cases, G_{12}, G_{13} and G_{23} have been calculated by Eqs. (2) and (3):

$$G_{12} = G_{13} = \frac{E_2}{2 \cdot (1 + \upsilon_{12})}, \tag{2}$$

$$G_{23} = \frac{E_2}{2 \cdot (1 + \upsilon_{23})}. \tag{3}$$

In order to examine the effect of material constants E_2 and E_3, a brief parameter study has been carried out. Material properties are the following in the case of E_2 = 200 MPa:

$$E_2 = E_3 = 200 \text{ MPa}, \ \nu_{12} = \nu_{13} = 0.2,$$
$$\nu_{23} = 0.4, \ G_{12} = G_{13} = 83 \text{ MPa}, \ G_{23} = 71 \text{ MPa}.$$

Results will be presented in Section 3.

The matrix is modeled by a 2 parameter Mooney-Rivlin model with parameters also mentioned in Section 2.2 'FE macromodel'.

The geometric model has shared topology which means that the whole FE model consists of one single mesh, being equal to perfectly bonded contacts between yarns and the matrix, and between each adjacent layers as well.

The FE model is a nonlinear model with large deflection (utilizing Cauchy stress tensor and Hencky logarithmic strain tensor [19]) using a nonlinear incremental approach.

The displacement coupling technique (also known as submodeling) matches the coupled surfaces of the micromodel (all the boundaries of the layers) with those of the macromodel using interpolation. In this study, the displacement coupling technique has been solely used to obtain the prescribed boundary conditions of the micromodel from the FE macromodel of the uniaxial tension of the standard test specimen as the difference between the average displacement of the right boundary (15.55 mm) and the average displacement of the left boundary (9.65 mm) in direction X.

Based on this, the displacements are the following: nodes of the right boundary translate 5.9 mm in direction X, having free degrees of freedom in direction Y and Z, shown in Fig. 8, while displacement of the nodes of the left boundary in direction X is 0 (Fig. 9). Weak springs ensure that any rigid body motion is avoided in directions Y and Z.

There are approximately 43200 nodes and 175400 SOLID185 elements (154000 4-node tetrahedral and 20300 8-node hexahedral elements) in the FE micromodel of the standard test specimen. This element type is homogeneous with full integration. The FE model has been created in ANSYS 2019 R1.

3 Results and discussion

Fig. 10 shows experimental force results, force results of the FE macromodel and force results of the FE micromodel

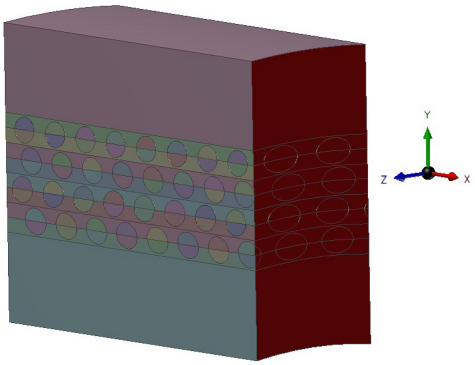

Fig. 8 Prescribed nodal displacement on the right boundary of the model (shown in red), undeformed shape

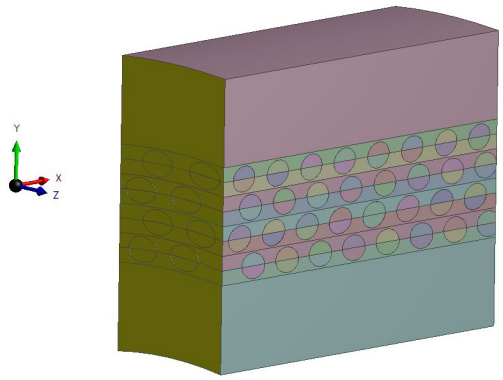

Fig. 9 Prescribed nodal displacement on the left boundary of the model (shown in yellow), undeformed shape

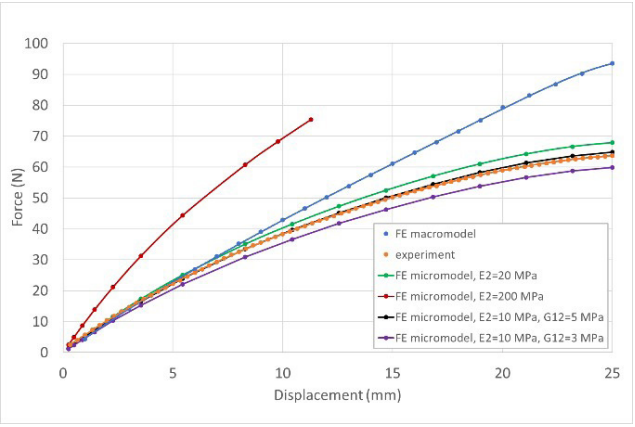

Fig. 10 Force-displacement curves of the standard test specimen; FE macromodel, experiment, FE micromodel at different moduli E_2 (10 MPa, 20 MPa, 200 MPa), G_{12}=5 MPa; and at E_2=10 MPa, G_{12}=3 MPa

at different moduli E_2 (10 MPa, 20 MPa, 200 MPa) at $G_{12} = 5$ MPa, and $E_2 = 10$ MPa at $G_{12} = 3$ MPa.

In case of modulus of elasticity $E_2 = 200$ MPa, the simulation has been convergent only until 11.28 mm ($E_2 = 200$ MPa) expressed as displacement of the FE macromodel. Force results of $E_2 = 20$ MPa are in good agreement with experimental results and they show similar tendencies, however, in case of $E_2 = 200$ MPa, the micromodel behaves much stiffer and force results are very far from the experimental results and have a different tendency.

Force results of $E_2 = 10$ MPa and $G_{12} = 5$ MPa are closer to experimental results than forces of $E_2 = 20$ MPa, forces measured at $E_2 = 10$ MPa and $G_{12} = 3$ MPa are lower than experimental results although these are still in an acceptable region. These results justify that despite the possible uncertainty associated with the estimation of elastic constants, experimental force results can be accurately approximated in the range of $E_2 = 10 \ldots 20$ MPa and

$G_{12} = 3…5$ MPa. By consequence, the applied parameters $E_2 = 20$ MPa and $G_{12} = 5$ MPa are acceptable for the modelling of tension of the composite test specimen.

Deformation, stress and strain results for the first reinforcement layer (and afterwards for other layers) in the images hereinafter presented are shown in the middle of the layer from top view (so the lower half of the layer is shown in these figures) at end time (at a displacement of 5.9 mm of the micromodel). All the deformation, strain and stress results are shown in the following images in deformation scale 1:1.

In these figures, the material coordinate system is displayed in the lower left corner, X, Y and Z indicating directions 1, 2 and 3.

Fig. 11 shows deformation in global X direction in the first layer. Deformation distribution is almost uniform regarding coordinates Z, this confirms that load distribution is even in terms of global longitudinal strains within the first layer.

In Figs. 12, 13, 14 and 15 strain components can be seen in material coordinate systems, firstly to the whole length (in Fig. 12), and then between $x = -4$ mm and $x = 4$ mm for the other components (Fig. 13, Fig. 14, Fig. 15). Right at the boundaries, high strain concentration can be seen due to the boundary effect (Fig. 12, Table 1) in very small areas. To overcome this issue, only the piece between $x = -4$ mm and $x = 4$ mm has been considered. All strain components are higher in the matrix than in yarns. Strains in material direction 1 (Fig. 12) are all positive,

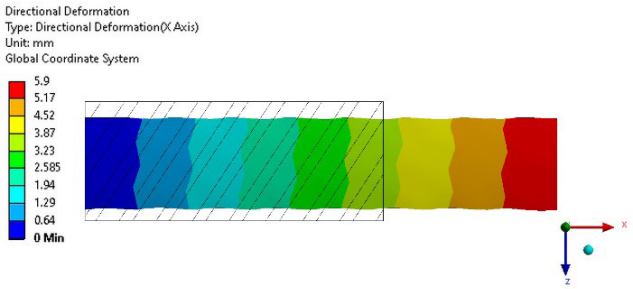

Fig. 11 Directional deformation (global X direction), *layer 1*

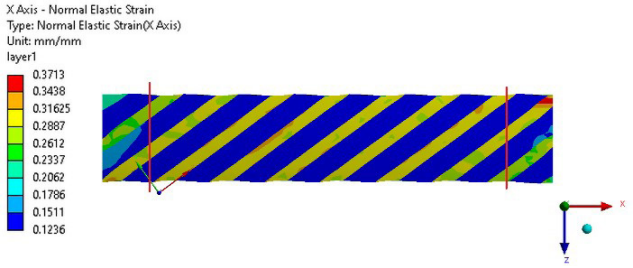

Fig. 12 Normal strain in material direction 1 in *layer 1*, (coordinates $x = -4$ mm and $x = 4$ mm shown with red lines)

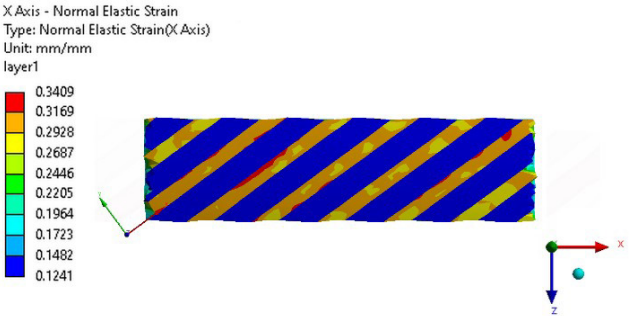

Fig. 13 Normal strain in material direction 1 in *layer 1* between $x = -4$ mm and $x = 4$ mm

Fig. 14 Normal strain in material direction 2 in *layer 1* between $x = -4$ mm and $x = 4$ mm

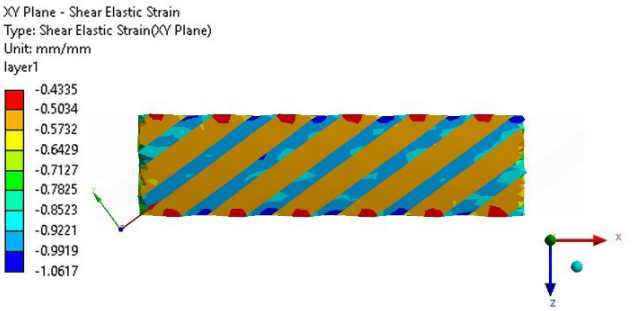

Fig 15 Shear strain in plane 12 in *layer 1* between $x = -4$ mm and $x = 4$ mm

matrix undergoes significant tension in this direction, while strains are not so significant in yarns due to high E_1.

In material direction 2, yarns sustain tension to a minor extent, while matrix is compressed to a greater extent (Fig. 14).

A significant difference can be seen between shear strains in plane 12 in yarns and matrix in Fig. 15. There are increased strains near free yarn ends (see the small red zones on the upper and the lower edges of the test specimen), this may lead to the conclusion that debonding is dominant in the failure mechanism of the cord-rubber reinforcement layers and that free yarn ends are probable initiation points of failure. Fig. 15 is in agreement with

Table 1 Maximum and minimum strains in each layer between x = -4 and +4 mm for the test specimen

	$\varepsilon_{1,\max}$ (-)	$\varepsilon_{1,\min}$ (-)	$\varepsilon_{2,\max}$ (-)	$\varepsilon_{2,\min}$ (-)	$\gamma_{12,\max}$ (-)	$\gamma_{12,\min}$ (-)
layer 1	0.349	0.1241	0.1332	−0.2542	−0.4335	−1.06
layer 2	0.3407	0.137	0.1639	−0.2462	1.0385	0.4437
layer 3	0.3369	0.1318	0.1332	−0.2245	−0.4525	−1.0779
layer 4	0.3387	0.1358	0.1162	−0.2198	1.1337	0.4815

Fig. 1, illustrating mechanical behaviour during the tensile test, where clearances can be seen near free yarn ends.

There is a considerable difference in shear strains γ_{12} between yarns and the matrix, which is numerically 0.55:0.95 (Fig. 16). High γ_{12} values imply that the dominant mode of load transfer is shear in the matrix in the reinforcement layers.

Fig. 16 shows strain components in material coordinate system in the path of Fig. 17. Strain ε_2 is the smoothest component being the smallest one. Strain component ε_1 is higher than ε_2. Shear strain γ_{12} values are higher even than ε_1 in the whole path.

Fig. 18 shows strain components in material coordinate system along yarn length (the exact path from which the results have been gathered can be seen in Fig. 19). These strain components are much lower than strains in the matrix. Strain component ε_1 is constant, strain ε_2 is small and strain γ_{12} is the most significant being much higher in absolute value than ε_1, confirming that yarns undergo significant shear while tension in material direction 1 is limited.

Fig. 20 shows stresses in material direction 1 in *layer 1*. Tensile stresses are equally distributed among yarns and matrix. Higher stresses arise firstly in the matrix and then the zone with higher stresses spreads in diagonal bands in yarns, resulting in a non-uniform stress distribution inside yarns, this can be attributed to the short-yarn reinforced nature of the test specimen.

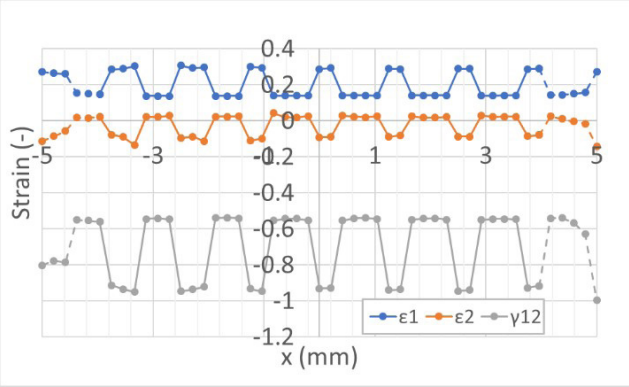

Fig. 16 Strains in material coordinate system along the path of Fig. 17 (in global direction X), the sections $x < -4$ mm and $x > 4$ mm are shown as dashed

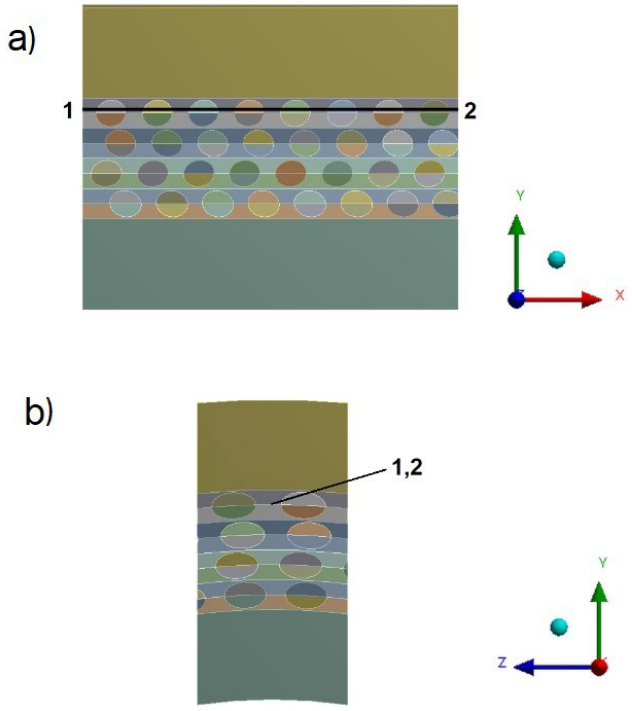

Fig. 17 Location of the path utilized for the visualization of stresses and strains in global direction X in the middle of *layer 1*; a) in plane XY; b) in plane YZ

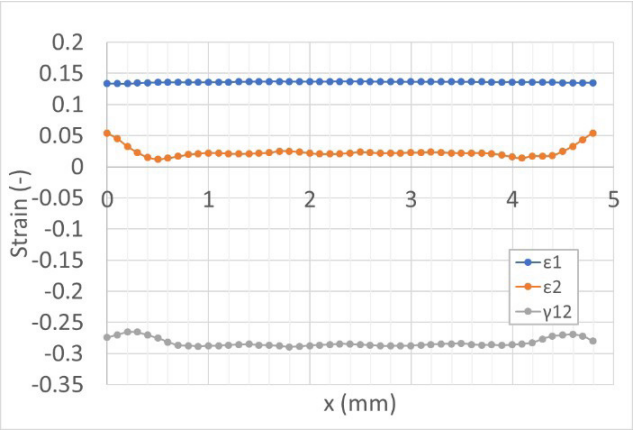

Fig. 18 Strain components in material coordinate system along yarn length

Fig. 21 shows stresses in material direction 2 in *layer 1* between $x = -4$ mm and $x = 4$ mm. Stress distribution in matrix and in the yarns is uniform, although stress in material direction 2 in yarns is not significant.

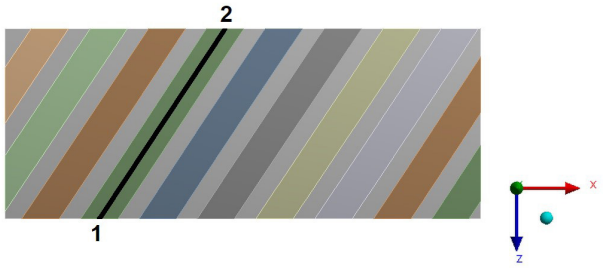

Fig. 19 Path in the middle of a yarn

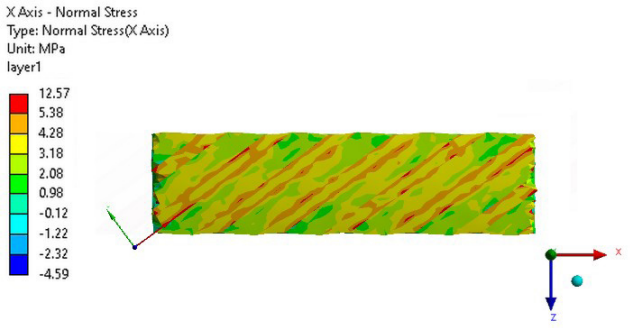

Fig. 20 Normal stress in material direction 1 in *layer 1* between $x = -4$ mm and $x = 4$ mm (with non-uniformly divided legend for better visualization)

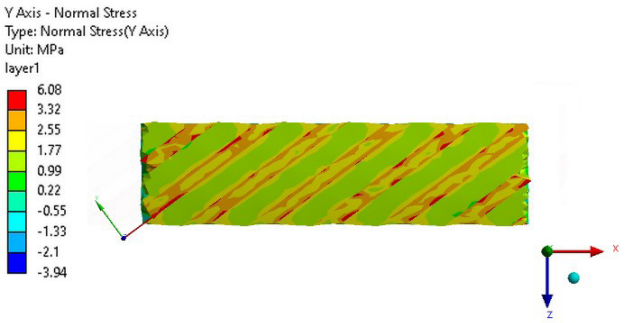

Fig. 21 Normal stress in material direction 2 in *layer 1* between x=-4 mm and x=4 mm (with non-uniformly divided legend for better visualization)

In Fig. 22, shear stresses in plane 12 in *layer 1* are shown between $x = -4$ mm and $x = 4$ mm. It shows higher negative shear stresses in the yarns and lower negative shear stresses in the matrix. τ_{12} is significant and relatively evenly distributed in yarns.

Fig. 23 shows stress components in material coordinate system along the path situated in the middle of *layer 1* (in terms of both vertical and horizontal dimensions), shown in Fig. 17, the zone affected by boundary effect is represented by dashed lines. Shear stress τ_{12} is the smoothest of all between $x = -4$ mm and $x = 4$ mm marking its principal significance in load transfer. Slightly higher stresses arise in yarns than in the matrix. On the other hand, σ_1 has the

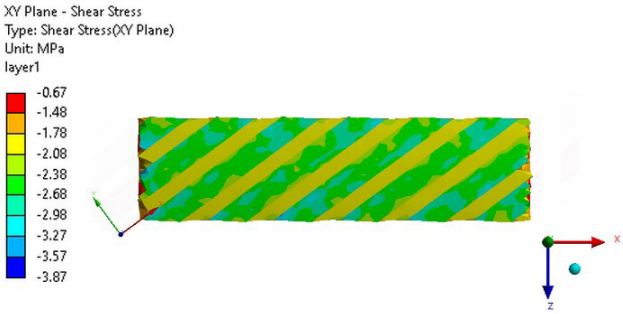

Fig. 22 Shear stress in plane 12 in layer 1 between $x = -4$ mm and $x = 4$ mm

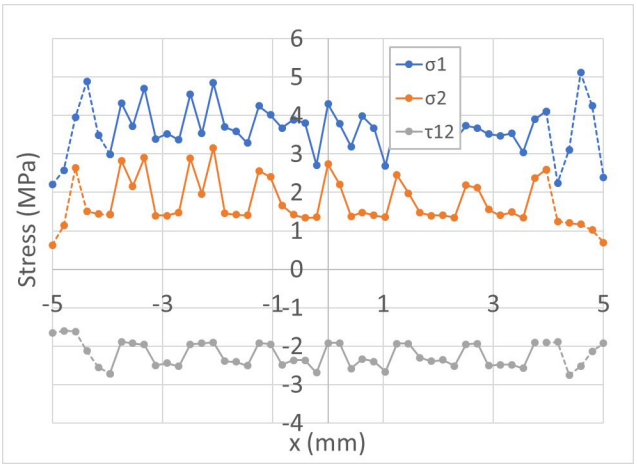

Fig. 23 Stress components in material coordinate system along the path of Fig. 17 (in global direction X), the sections $x < -4$ mm and $x > 4$ mm are shown as dashed

highest differences between values of the yarns and the matrix, having a slightly higher maximum than σ_2.

For examination of stresses along yarns, stress results have been plotted in Fig. 24 along a path in the middle of the yarn, shown in Fig. 19. The entire path is situated outside the regions affected by the boundary effect. Inside one yarn, tensile stresses in material direction 1 oscillate

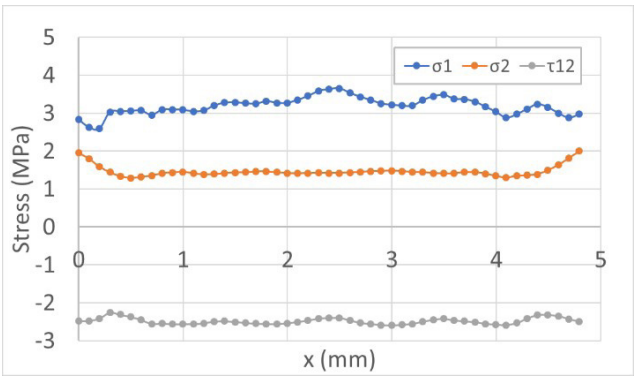

Fig. 24 Stress components in the path of Fig. 19 in material coordinate system along yarn length

between 3 MPa and 3.65 MPa, having larger range than σ_2 and τ_{12}, further confirming that stress distribution in material direction 1 is not uniform in yarns. High shear stresses τ_{12} arise even in the yarns being as significant as normal stresses σ_1. As it can be seen in Fig. 24, only tensile stresses occur in yarns in material direction 1 and 2, so it is enough to focus only on tensile moduli in the material model of the yarns. This statement is also confirmed by Fig. 13 and Fig. 14.

Among the stresses in all the layers in the zone not affected by boundary effect between x = −4 mm and x = 4 mm (Table 2), tensile stresses in material direction 1 are the most significant, while stresses in material direction 2 and shear stresses τ_{12} are also substantial confirming that tension-shear coupling is prominent in the mechanical behaviour of the composite test specimen.

Fig. 25 displays yarn orientation angles (of yarns 1, 2, 3, 4, 5, 6, 7, 8 and 9 designated in Fig. 26) during FE simulation as a variance of displacement. As displacement increases and the test specimen elongates, yarn orientation angles decrease as an approximately linear function of displacement because of the contraction of the cross-section.

In reinforcement layers in the matrix, shear dominates the mechanical behavior in the midplane of reinforcement layers both in terms of strains and stresses (Figs. 27, 28 and 29), representing similar behaviour as in *layer 1* (Figs. 15 and 22).

In Fig. 30, positive shear strain values arise in the zones where there are no overlapping yarns in adjacent layers. In these zones, in-plane shear transmits load between the adjacent reinforcement layers. The lowest shear strains occur in zones where there are overlapping yarns in adjacent layers. Fig. 31 shows shear stresses between *layer 1* and *layer 2*, having the same tendency as Fig. 30.

4 Conclusion

FE micromechanical analysis of cord-rubber composite tube test specimen presented in this article is based on an incremental large deflection technique and is established with the utilization of submodeling. The material model is elastic, moduli of elasticity E_2 and E_3 and shear moduli

Table 2 Maximum and minimum stresses in each layer between $x = -4$ mm and $x = 4$ mm for the test specimen

	$\sigma_{1,\max}$ (MPa)	$\sigma_{1,\min}$ (MPa)	$\sigma_{2,\max}$ (MPa)	$\sigma_{2,\min}$ (MPa)	$\tau_{12\max}$ (MPa)	$\tau_{12\min}$ (MPa)
layer 1	11.75	−3.82	6.08	−3.94	−0.37	−4.6
layer 2	16.73	−4.73	6.9	−5.68	4.63	−0.32
layer 3	12.57	−3.42	6.76	−2.88	0.01	−4.69
layer 4	11.59	−3.65	6.47	−4.05	4.13	0.53

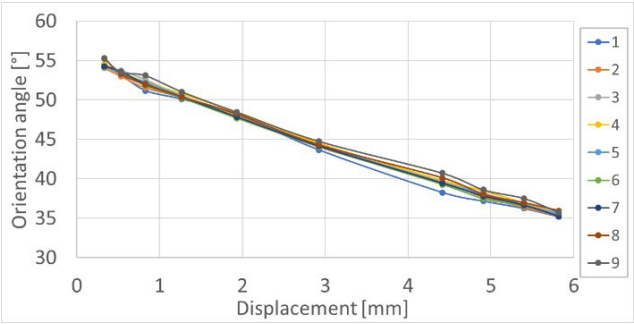

Fig. 25 Yarn orientation angles during FE simulation

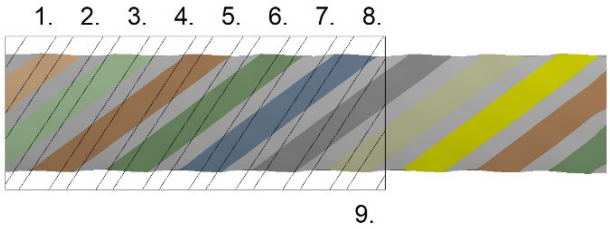

Fig. 26 Yarn orientation angles at the end of the simulation, the undeformed shape and initial yarn orientation is shown in black

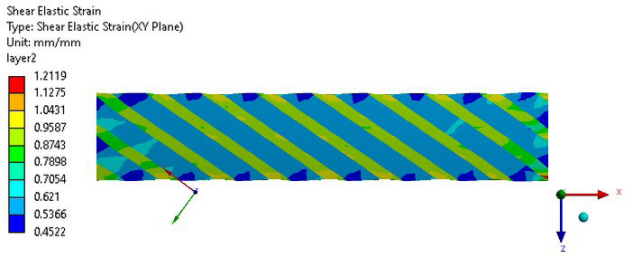

Fig. 27 Shear strain in plane 12 in *layer 2*

Fig. 28 Shear strain in plane 12 in *layer 3*

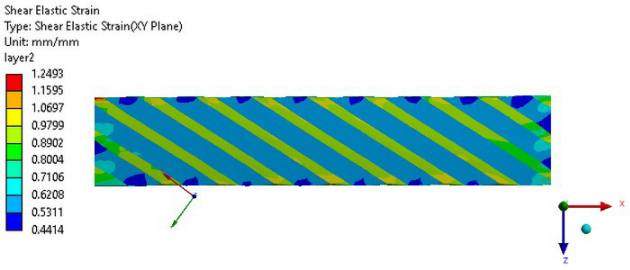

Fig. 29 Shear strain in plane 12 in *layer 4*

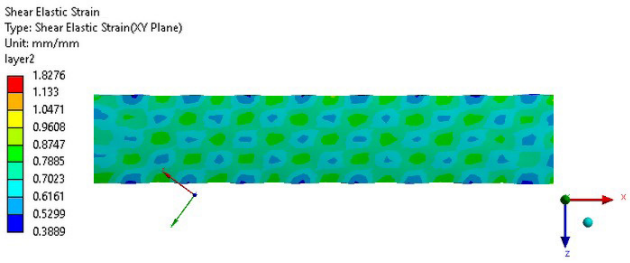

Fig. 30 Shear strain between *layer 1* and *layer 2*, at the top of *layer 2*

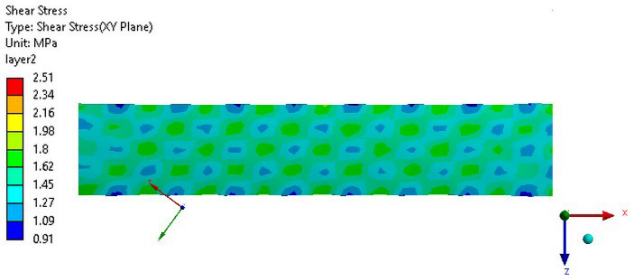

Fig. 31 Shear stress between *layer 1* and *layer 2*, at the top of *layer 2*

G_{12}, G_{23} and G_{13} are estimated and the element sizes may induce some inaccuracy. At the same time, the stress-strain results represent only tension. The main conclusions are as follows:

1. Force-displacement curves of the micromodel and experimental results show a considerably good agreement. In both cases, $E_2 = E_3 = 20$ MPa approximate experimental results accurately, however, significantly higher moduli ($E_2 = E_3 = 200$ MPa), overestimate tensile reaction forces significantly.
2. Stress distribution in material direction 1 is non-uniform in yarns, forming bands with higher stresses going through the yarns, while stress-distribution in the matrix is nearly uniform. Load transfer to the yarns is quite poor, because of the short-yarn reinforced nature of the specimen (due to the low width of the specimen) and because orientation angle of the composite tube is 55°, which is optimal for biaxial tension (uniaxial tension and pressure), so the tensile load is not entirely carried by yarns, instead, the matrix has a larger role in bearing the load, which is not characteristic to composite structures in general. The shear plays an important role in load transfer and also in failure mechanism of the specimen. Shear strains are high at free yarn ends marking the possible locations of failure initiation in debonding in the shear mechanism of the reinforcement layers (see $\gamma_{12\max}$, $\gamma_{12\min}$ in Table 1). Shear strain γ_{12} values are higher even than ε_1 in the whole longitudinal path of Fig. 17.
3. There is a considerable difference in strains between yarns and the matrix. This is the most perceptible in the case of strain γ_{12}, which is numerically 0.55:0.95. High γ_{12} values imply that the dominant mode of load transfer is shear in the reinforcement layers.

Regarding stresses, there is a large difference between values in the matrix and the yarns.

Acknowledgement

The research reported in this paper is part of project no. BME-NVA-02, implemented with the support provided by the Ministry of Innovation and Technology of Hungary from the National Research, Development and Innovation Fund, financed under the TKP2021 funding scheme.

References

[1] Braiek, S., Zitoune, R., Ben Khalifa, A., Zidi, M. "Experimental and numerical study of adhesively bonded ±55° filament wound tubular specimens under uniaxial tensile loading", Composite Structures, 172, pp. 297–310, 2017. https://doi.org/10.1016/j.compstruct.2017.03.103

[2] Almeida Jr., J. H. S., Ribeiro, M. L., Tita, V., Amico, S. C. "Damage modeling for carbon fiber/epoxy filament wound composite tubes under radial compression", Composite Structures, 160, pp. 204–210, 2017. https://doi.org/10.1016/j.compstruct.2016.10.036

[3] Carroll, M., Ellyin, F., Kujawski, D., Chiu, A. S. "The rate-dependent behaviour of ±55° filament-wound glass-fibre/epoxy tubes under biaxial loading", Composites Science and Technology, 55(4), pp. 391–403, 1995. https://doi.org/10.1016/0266-3538(95)00119-0

[4] Kwak, S. B., Choi, N. S. "Micro-damage formation of a rubber hose assembly for automotive hydraulic brakes under a durability test", Engineering Failure Analysis, 16(4), pp. 1262–1269, 2009. https://doi.org/10.1016/j.engfailanal.2008.08.009

[5] Soden, P. D., Kitching, R., Tse, P. C., Tsavalas, Y., Hinton, M. J. "Influence of winding angle on the strength and deformation of filament-wound composite tubes subjected to uniaxial and biaxial loads", Composites Science and Technology, 46(4), pp. 363–378, 1993. https://doi.org/10.1016/0266-3538(93)90182-G

[6] Liu, N., Wenbin, Y. "Evaluation of smeared properties approaches and mechanics of structure genome for analyzing composite beams", Mechanics of Advanced Materials and Structures, 25(14), pp. 1171–1185, 2018. https://doi.org/10.1080/15376494.2017.1330977

[7] Rosso, P., Váradi, K. "FE macro/micro analysis of thermal residual stresses and failure behaviour under transverse tensile load of VE/CF – fibre bundle composites", Composites Science and Technology, 66(16), pp. 3241–3253, 2006. https://doi.org/10.1016/j.compscitech.2005.07.004

[8] Violeau, D., Ladevèze, P., Lubineau, G. "Micromodel-based simulations for laminated composites", Composites Science and Technology, 69(9), pp. 1364–1371, 2009. https://doi.org/10.1016/j.compscitech.2008.09.041

[9] Llorca, J., González, C., Molina-Aldareguía, J. M., Segurado, J., Seltzer, R., Sket, F., Rodríguez, M., Sádaba, S., Muñoz, R., Canal, L. P. "Multiscale Modeling of Composite Materials: a Roadmap Towards Virtual Testing", Advanced Materials, 23(44), pp. 5130–5147, 2011. https://doi.org/10.1002/adma.201101683

[10] Arteiro, A., Catalanotti, G., Reinoso, J., Linde, P., Camanho, P. P. "Simulation of the Mechanical Response of Thin-Ply Composites: From Computational Micro-Mechanics to Structural Analysis", Archives of Computational Methods in Engineering, 26, pp. 1445–1487, 2019. https://doi.org/10.1007/s11831-018-9291-2

[11] Xu, K., Qian, X., Duan, D., Chen, B., Guo, L. "A novel macro-meso finite element method for the mechanical analysis of 3D braided composites", Mechanics of Materials, 126, pp. 163–175, 2018. https://doi.org/10.1016/J.MECHMAT.2018.08.007

[12] Zhang, C., Li, N., Wang, W., Binienda, W. K., Fang, H. "Progressive damage simulation of triaxially braided composite using a 3D meso-scale finite element model", Composite Structures, 125, pp. 104–116, 2015. https://doi.org/10.1016/j.compstruct.2015.01.034

[13] Li, D., Lu, Z., Chen, L., Li, J. "Microstructure and mechanical properties of three-dimensional five-directional braided composites", International Journal of Solids and Structures, 46(18–19), pp. 3422–3432, 2009. https://doi.org/10.1016/j.ijsolstr.2009.05.013

[14] Szabó, G., Váradi, K., Felhős, D. "Finite Element Model of a Filament-Wound Composite Tube Subjected to Uniaxial Tension", Modern Mechanical Engineering, 7(4), pp. 91–112, 2017. https://doi.org/10.4236/mme.2017.74007

[15] Szabó, G., Váradi, K., Felhős, D. "Bending Analysis of a Filament-Wound Composite Tube", Modern Mechanical Engineering, 8(1), pp. 66–77, 2018. https://doi.org/10.4236/mme.2018.81005

[16] Kim, B., Lee, S. B., Lee, J., Cho, S., Park, H., Yeom, S., Park, S. H. (2012) "A comparison among Neo-Hookean model, Mooney-Rivlin model, and Ogden model for chloroprene rubber", International Journal of Precision Engineering and Manufacturing, 13(5), pp. 759–764, 2012. https://doi.org/10.1007/s12541-012-0099-y

[17] Karger-Kocsis, J., Mousa, A., Major, Z., Békési, N. "Dry friction and sliding wear of EPDM rubbers against steel as a function of carbon black content", Wear, 264(3–4), pp. 359–367, 2008. https://doi.org/10.1016/j.wear.2007.03.021

[18] Behroozinia, P., Taheri, S., Mirzaeifar, R. "An investigation of intelligent tires using multiscale modeling of cord-rubber composites", Mechanics Based Design of Structures and Machines, 46(2), pp. 168–183, 2018. https://doi.org/10.1080/15397734.2017.1321488

[19] Kohnke, P. (ed.) "Large strains", In: ANSYS Mechanical APDL Theory Reference, ANSYS, Inc., Canonsburg, PA, USA, 2013, pp. 29–35.